Clinical Epigenetics

RESEARCH

Open Access

Radiogenomic method combining DNA methylation profiles and magnetic resonance imaging radiomics predicts patient prognosis in skull base chordoma

Xiaoyu Deng[1†], Peiran Li[2†], Kaibing Tian[2†], Fan Zhang[1], Yumeng Yan[1], Yanghua Fan[2], Zhen Wu[2], Junting Zhang[2], Jiang Du[3*], Wei Chen[1*] and Liang Wang[2*]

Abstract

Background Chordoma is a rare malignant bone tumor exhibiting poor survival and prognosis. Hence, it is crucial to develop a convenient and effective prognostic classification method for the rehabilitation and management of patients with chordoma. In this study, we combined DNA methylation profiles and magnetic resonance imaging (MRI) images to generate a radiogenomic signature to assess its effectiveness for prognosis classification in patients with skull base chordoma.

Results DNA methylation profiles from chordoma tissue samples of 40 patients were factorized into eight DNA methylation signatures. Among them, Signature 4 was identified as the prognosis-specific signature. Based on the Signature 4 loading values, the patients were categorized into low-signature (LLG) and high-signature (HLG) loading groups. HLG patients had higher progression-free survival times than LLG patients. Combined analysis with external single-cell RNA-seq data revealed higher tumor cell proportions and lower natural killer cell proportions in the HLG than in the LLG. Additionally, 2,553 radiomic features were extracted from T1, T2, and enhanced T1 MRI images of the patients, and a radiogenomic signature comprising 14 radiomic features was developed. In a validation cohort of 122 patients, the radiogenomic signature successfully distinguished between the two groups ($P=0.027$). Furthermore, the existence of Signature 4 was confirmed in an additional dataset of 14 patients.

Conclusion We developed a prognostic radiogenomic signature using a radiogenomic classification method, which leverages MRI images to extract features that reflect the DNA methylation signature associated with prognosis, enabling the stratification of patients based on their prognostic risk. This method offers the advantages of being noninvasive and convenient.

Keywords Chordoma, Radiogenomics, DNA methylation signature

†Xiaoyu Deng, Peiran Li, and Kaibing Tian have equally contributed to this work.

*Correspondence:
Jiang Du
duxiangyi2003@sina.com
Wei Chen
chenw123@buaa.edu.cn
Liang Wang
saintage7@126.com

Background

Chordoma is a rare malignant bone tumor arising from embryonic notochord. It primarily affects the axial skeleton, particularly the skull base, sacrococcygeal region, and mobile spine [1, 2], and accounts for 1–4% of all bone malignancies, with an incidence of about 0.08/100,000 [3]. Due to its specific location, the tumor often causes local bone destruction and compression of surrounding structures during its growth, causing symptoms such as local pain and nerve invasion [2, 4, 5]. Despite its slow growth, chordoma exhibits strong local aggressiveness and a propensity for distant metastasis [6]. This delayed detection due to advanced stage at diagnosis further hinders treatment efficacy. The high mortality rate associated with chordoma is concerning, with 5-, 10-, and 20-year survival rates dropping dramatically to 67.6%, 39.9%, and 13.1%, respectively [3, 6]. Additionally, over 50% of patients experience recurrence despite undergoing surgery and radiotherapy [7].

The high mortality and recurrence rates of chordoma highlight the critical need to elucidate its molecular mechanisms. Currently, genomic [8–10] and transcriptomic [11–15] studies have identified various genes and pathways associated with chordoma, providing valuable insights for clinical research and treatment development. DNA methylation profiling, an emerging tool for cancer diagnosis and classification [16], has also been used to distinguish chordoma subtypes [17–19]. However, obtaining biopsy samples harms patients' bodies and acquiring DNA methylation profiles of tumor samples is time-consuming, hindering its use for preoperative prediction in routine clinical diagnosis.

Medical imaging is a noninvasive and low-cost method for clinical diagnosis that provides extensive information without harming the patient. Radiomic features extracted from medical images can determine genomic changes within tumor cells [20]. This has paved the way for radiogenomics, a technique that combines genomics and radiomics to analyze disease diagnosis, stratification, and prognosis at a molecular level, all in a noninvasive and convenient manner [21–25]. Magnetic resonance imaging (MRI) is a widely used medical imaging tool for chordoma diagnosis and study. This study aimed to establish a link between MRI images and DNA methylation profiles to extract epigenetic information noninvasively from medical images. By first identifying a chordoma prognosis-specific DNA methylation signature, we can then combine this information with patients' MRI data through radiomic analysis to construct a radiogenomic signature. This signature has the potential to predict patient prognosis noninvasively, facilitating its application in routine clinical diagnosis.

Materials and methods

Patient cohort

This study enrolled 176 patients with skull base chordoma, who were categorized into three independent cohorts (Supplementary Fig. 1). The first cohort (the discovery cohort) comprised 40 patients with preoperative MRI images and tumor samples to obtain DNA methylation profiles. The second cohort (the methylation validation cohort) comprised 14 patients with MRI images and formalin-fixed paraffin-embedded (FFPE) tumor tissues. The third cohort (the radiomic validation cohort) comprised 122 patients with a full series of MRI images. The Ethics Committee of Beijing Tiantan Hospital approved this study, and all patients signed written informed consent forms for the study. All patients received telephone or clinical follow-up before December 2024.

Methylation profiling of chordoma tissues

We extracted DNA from both fresh-frozen (40 samples in discovery cohort) and FFPE tissues (14 samples in methylation validation cohort) using the Qiagen DNA Mini Kit (Qiagen, Hilden, Germany), following the manufacturer's protocol. FFPE-derived DNA underwent an additional repair process using Infinium FFPE QC and DNA Restoration Kits (Illumina, San Diego, CA). For bisulfite conversion, 400 ng of DNA from each sample was processed using the EZ DNA Methylation Kit (Zymo research, Irvine, CA). Subsequently, methylation levels were detected using either the Infinium Methylation 450 K (fresh-frozen tissues) or the Methylation EPIC BeadChip array (Illumina, San Diego, CA) (FFPE tissues), depending on the sample cohort.

The quality of array data was assessed using the ChAMP package [26, 27]; CpG sites located on the X or Y chromosomes, those overlapping or flanked by single-nucleotide polymorphisms, and those with detection $p > 0.0001$ were removed. The idat files underwent processing via ChAMP, followed by data normalization using the champ.norm function. Finally, we calculated the variance of each CpG site across all samples within the DNA methylation profiles of 40 patients. CpG sites exhibiting a variance exceeding 0.05 were identified as the most variably methylated CpG sites for subsequent studies.

DNA methylation signature associated with prognosis

We employed nonnegative matrix factorization (NMF) on the most variably methylated CpG sites from our 40 patient samples using the NMF package [28]. The optimal number of factors (methylation signatures) was determined based on a cophenetic diagram analysis. This process decomposed the CpG sites into distinct methylation signatures, highlighting the critical CpG sites (meta CpG sites) contributing most significantly to each

signature. Next, we analyzed each methylation signature in relation to patient progression-free survival (PFS) data. The surv_cutpoint function within the R package survminer [29] was used to stratify the 40 samples into the high-signature [HLG] and low-signature [LLG] loading groups. This approach, which combines PFS data and the identified methylation signature loading values, avoids the bias associated with manual stratification. Kaplan–Meier curves were then generated to visualize differences in PFS between the HLG and LLG. We defined signatures with a statistically significant association with PFS (false discovery rate [FDR] <0.01) as prognosis-specific. Subsequently, the identified prognosis-specific signature along with its corresponding two groups were analyzed for their functional relevance.

We selected 700 differentially methylated probes (DMPs), encompassing the top and bottom 350 sites with the highest absolute delta β and $p<0.05$, respectively. These DMPs represented the most pronounced methylation differences between the HLG and LLG. We then identified the genes associated with these DMPs and performed a functional enrichment analysis for Gene Ontology (GO) terms using the ClusterProfiler R package [30] to understand the biological processes potentially impacted by differential methylation within each group.

Radiomic feature extraction and radiomic signature building

The regions of interest were manually outlined on the T1, T2, and contrast-enhanced T1 sequence MRI images in the Digital Imaging and Communications in Medicine (DICOM) format using ITK-SNAP (version 4.0.0). For each patient in the discovery cohort, a total of 2,553 radiomic features were extracted from these images using the 'PyRadiomics' package [31] in Python. There were 851 features extracted from each sequence, which were broadly categorized into 1) first-order statistics features ($n=18$); 2) shape-based (2D and 3D) features ($n=14$); 3) textural features derived from texture matrices, including gray level co-occurrence matrix, gray level run length matrix, gray level size zone matrix, gray level dependence matrix, and neighboring gray tone difference matrix ($n=75$); and 4) filter-derived features: wavelet ($n=744$).

After z-score scaling the radiomic features, Pearson correlation coefficients were first calculated to identify features significantly correlated ($p<0.05$) with the selected methylation signature in the discovery cohort, aiming to select the most relevant features. Then, the least absolute shrinkage and selection operator (LASSO) regression was applied to further refine the selected features and address the issue of multicollinearity [32]. To optimize data utilization and determine the hyperparameters for LASSO regression, fivefold cross-validation was employed [33]. The coefficients of LASSO regression for selected features were applied to calculate a radiogenomic signature for each patient. This signature served as a novel categorical biomarker for predicting the DNA methylation signature groups and chordoma prognosis. The scikit-learn library facilitated our analysis in this section [34].

Validation of DNA methylation signature prevalence across diverse datasets and its prognostic correlation

The effectiveness of the radiogenomic signature obtained from the discovery cohort was validated using two external validation cohorts. Our validation focused on two key aspects: (1) assessing the generalizability of the selected signature across different datasets and (2) confirming that the selected signature was specific to prognosis.

For the methylation validation cohort, we evaluated the radiogenomic signature's ability to predict DNA methylation signatures, confirming its consistency across different datasets. Radiomic features were first extracted from patient scans in this cohort and then normalized using the mean and standard deviation values of features from the discovery cohort. Next, the coefficients derived from the discovery cohort were applied to compute the radiogenomic signature for each patient in the validation cohort. Patients were subsequently stratified into methylation validation high and low signature loading groups (mv-HLG and mv-LLG groups) based on their signature values. Due to differences between 450 K and EPIC methylation microarrays, as well as differences between fresh-frozen and FFPE tissues, we employed different approaches for CpG site analysis in the cohorts: For the discovery cohort, the 350 most variably methylated CpG sites from the two groups were selected for analysis, whereas for the validation cohort, all CpG sites were included. Gene set enrichment analysis (GSEA) was performed using GSEA software to compare the enrichment patterns of all CpG sites between the two groups in the validation cohort across the two 350 CpG site lists [35, 36].

In the radiomic validation cohort, we investigated the broader applicability and prognostic value of the signature. Radiomic features were extracted, normalized, and used to calculate radiogenomic signature values for 122 patients in this cohort. Patients were then stratified into two groups based on their signature values. Kaplan–Meier curves and log-rank tests were employed to compare survival outcomes between the two groups. The aim was to determine if the observed trends mirrored those seen in the discovery cohort, supporting the prognostic relevance of the radiogenomic signature.

Deconvolution of DNA methylation profiles using external scRNA-seq data

To gain further insights into functional differences between the prognosis groups in the discovery cohort (i.e., 40 patients) at the single-cell level, we analyzed an independent single-cell RNA-sequencing (scRNA-seq) dataset from six patients with chordoma [37]. We employed the Seurat package [38] (version 4.0.6) to perform quality control, dimensionality reduction, and cluster analysis on the single-cell transcriptome data. Cell types were manually annotated based on specific cell-type markers and SingleR [39] annotation results. Subsequently, we generated a gene list based on the top 1500 differential methylated CpG sites ($p < 0.05$) within each group. The average expression levels of these genes were then computed across various cell types in the scRNA-seq data using the AddModuleScore function in Seurat. Cell–cell communication patterns between various cell types were analyzed using the CellChat package [40]. Finally, we leveraged scRNA-seq data using the EpiSCORE [41] package, which enabled us to deconvolute the DNA methylation profiles to estimate their cell-type compositions. This analysis enabled us to compare the cell-type proportions between the prognosis-specific signature groups.

Multiplex immunofluorescence histochemistry (mIHC) staining and cell proportion calculation

Samples from 12 patients were selected from the discovery cohort, and mIHC staining was performed. These samples were previously preserved in paraffin wax. Following the manufacturer's instructions for the Absin Kit (abs50013), we processed the paraffin-embedded sections through mIHC staining. In brief, the sections were first dewaxed with xylene and rehydrated with ethanol, followed by antigen retrieval. The designated areas of the tissue sections were marked, followed by washing in PBST and blocking with H_2O_2 and serum. The remaining liquid on the slide was removed, the primary antibody was added, and sections were incubated at room temperature, followed by addition of the HRP secondary antibody solution. The slide was washed with TBST and the dye working solution was added and incubated. After staining all target proteins, the nuclei were stained using DAPI. Anti-fluorescence quenching sealing agent was applied, and the slide was sealed with a cover glass. Finally, the sections were examined under PhenoImager (Akoya Biosciences) and processed using Phenochart software. DAPI staining identified all cell nuclei, whereas FITC, TEXAS-RED, and CY5 identified cells expressing CD16, CD56, and CD3 proteins, respectively. The stained images were processed using Fiji [42].

Statistical analyses

Statistical analyses and data visualizations were performed using R software (version 4.2.2). Kaplan–Meier curves were compared using log-rank tests. Categorical variables were analyzed using Fisher's exact tests, while continuous variables were assessed with t tests. The overall workflow is illustrated in Supplementary Fig. 1.

Results

Chordoma patient cohort

The discovery cohort comprised 40 patients, of whom 12 (30%) experienced disease progression during follow-up. The median PFS time for patients who progressed was 48.5 months, whereas that for censored patients (those who did not experience progression during the follow-up period) was 112.5 months. In the methylation validation cohort, five (35.7%) patients experienced progression during follow-up, whereas in the radiomic validation cohort, 11 (13.1%) patients experienced progression. Details on PFS times for all cohorts are presented in Table 1. We reviewed patient records and collected various clinical factors potentially associated with chordoma, including age, gender, extent of tumor resection, type of bone and dural invasion, tumor blood supply, and past tumor history. The analysis revealed no statistically significant differences in these factors between patients who experienced progression and those who did not.

Identification of DNA methylation signatures

To understand the DNA methylation signatures in chordoma tissues, we analyzed 407,014 CpG sites from 40 patients using the Illumina Methylation 450 K chip. We identified 1,334 CpG sites exhibiting the highest variability (variance of β value > 0.05). Next, we employed NMF to extract DNA methylation signatures from these variable CpG sites (Fig. 1A). Then, the most variable methylated sets were factorized into eight DNA methylation signatures in the discovery cohort. Notably, the same methylation sites were present in varying proportions across these different signatures. Each patient sample exhibited a unique loading value for all eight signatures (Fig. 1B). We then divided the 40 samples into two groups for each signature based on their corresponding loading value (Supplementary Fig. 2). Samples with higher loading values were assigned to the HLG, whereas those with lower loading values were designated as the LLG. Subsequently, survival analysis was performed on these groups (Fig. 1C–J). Kaplan–Meier plots revealed significant differences ($p < 0.05$) in PFS for groups defined by Signature 2, 4, 5, and 6. However, after applying FDR correction for multiple comparisons, only Signature 4 retained a statistically significant adjusted p value (Table 2). Patients in the HLG for Signature 4 had a better prognosis than

Table 1 Clinical and pathological characteristics of patients

	Discovery cohort				Methylation validation cohort				Radiomic validation cohort			
	All (N = 40)	Progression (n = 12)	No progression (n = 28)	*P*	All (N = 14)	Progression (n = 5)	No progression (n = 9)	*P*	All (N = 122)	Progression (n = 16)	No progression (n = 106)	*P*
Age, mean (range)	34.7(11–67)	37.8(22–63)	33.4(11–67)	0.377	38.6(10–63)	42.6(31–49)	36.3(10–63)	0.383	37.5(5–66)	38.3(15–66)	37.4(5–66)	0.799
Gender				0.729				1				0.789
Male	24	8	16		10	4	6		73	9	64	
Female	16	4	12		4	1	3		49	7	42	
Extension of resection				0.581				0.059				0.34
100%	3	0	3		2	0	2		18	2	16	
90–100%	23	6	17		9	2	7		79	11	68	
70–90%	11	5	6		2	2	0		19	1	18	
< 70%	3	1	2		1	1	0		6	2	4	
Bone invasion				1				0.221				1
Exophytic type	30	10	20		10	5	5		94	13	81	
Endophytic type	2	0	2		0	0	0		6	0	6	
Intrinsic type	8	2	6		4	0	4		22	3	19	
Dural invasion				1				0.221				0.284
Subdural	23	7	16		4	3	1		46	8	38	
Epidural	17	5	12		9	2	7		76	8	68	
Unknown	0	0	0		1	0	1		0	0	0	
Blood supply				0.165				0.086				0.154
Abundant	22	9	13		8	4	4		71	13	58	
Moderate	18	3	15		5	0	5		50	3	47	
Poor	0	0	0		1	1	0		1	0	1	
Tumor history				1				1				0.511
No	39	12	27		14	5	9		117	15	102	
Yes	1	0	1		0	0	0		5	1	4	
PFS (months), median (range)	111.5 (4–165)	48.5 (4–152)	112.5 (8–165)	0.041	57.5 (8–86)	27 (8–63)	60 (11–86)	0.072	61.5 (3–204)	33.5 (11–105)	67.5 (3–204)	0.004

P values are the result of Fisher's exact tests (categorical variables) or t tests (continuous variables)

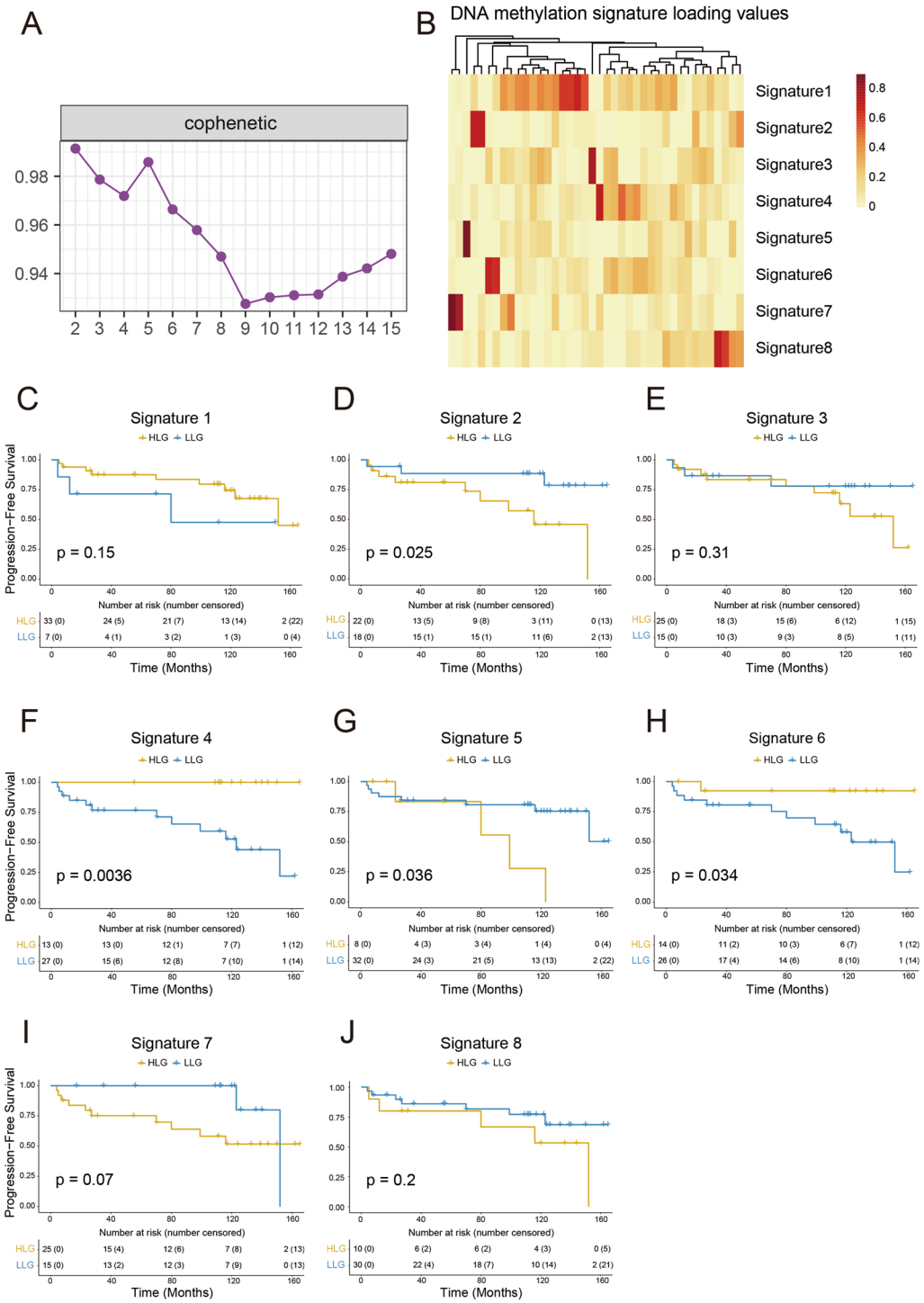

Fig. 1 Selection of the prognosis-specific signature. **A** Cophenetic correlation coefficients plot of NMF across the factorization ranks ranging from 2 to 15. **B** Loading values of each DNA methylation signature. **C**–**J** Progression-free survival stratified by methylation groups in the discovery cohort. Kaplan–Meier curves showing progression-free survival in patients. The two curves are compared using the log-rank test

those in the LLG. Therefore, Signature 4 was selected as the signature of interest for further investigation due to its prognostic significance.

To explore functional differences between the two prognosis-specific signature groups defined by Signature 4, we performed an overrepresentation analysis on the

Table 2 *P* values and adjusted *p* values of log-rank tests for survival curves of the two groups

DNA methylation signature	*p* value	adjusted *p* value
Signature 1	0.15	0.2
Signature 2	0.025	0.072
Signature 3	0.31	0.31
Signature 4	0.0036	0.0288
Signature 5	0.036	0.072
Signature 6	0.034	0.072
Signature 7	0.07	0.112
Signature 8	0.2	0.2286

700 CpG sites ($p < 0.05$, delta $\beta > 0.18$ in HLG and < -0.24 in LLG) exhibiting the greatest methylation variation within this signature (Fig. 2A, B). Genes associated with activation of adaptive immune cells were found to be hypermethylated in the HLG ($p < 0.012$), suggesting a potential link between adaptive immunity and prognosis. Conversely, genes related to cell growth, development, and negative regulation of the TGF-β pathway were hypermethylated in the LLG ($p < 0.036$), implying a possible role for the TGF-β pathway in chordoma prognosis.

Radiogenomic signature construction

We next investigated the potential of radiomic features to predict the values corresponding to Signature 4. Within the discovery cohort, we identified 14 radiomic features exhibiting the strongest correlation with Signature 4 from a pool of 2,553 features (details in Supplementary Table 1). These features were then used to construct a radiogenomic signature score. A score threshold of 0.24 was established to differentiate between the HLG and LLG within the discovery cohort. Patients with scores below this threshold were classified into the LLG, while those with scores above the threshold were classified into the HLG. The radiogenomic signature score emerged as a significant predictor of prognosis, with patients in the two groups exhibiting statistically different survival outcomes ($P = 0.0014$), as shown in Fig. 2C.

Validation of the generalizability of DNA methylation signature 4 across different datasets

To assess the generalizability of Signature 4 across different datasets, we employed a methylation validation cohort consisting of 14 patients with FFPE tissue analyzed using the Illumina EPIC methylation array. Using the radiogenomic signature scores, we classified 11 patients into the mv-HLG and three into the mv-LLG. Two out of three patients from the mv-LLG group and three out of 11 patients from mv-HLG group showed progression during follow-up. GSEA results (Fig. 2D, E) revealed that CpG sites in the mv-LLG were enriched within the list of top 350 hypermethylated CpG sites identified in the LLG of the discovery cohort ($p < 0.01$). This finding suggests consistent methylation signatures across these different datasets. Although the mv-HLG did not show significant enrichment in in the top 350 hypermethylated CpG sites of the HLG from the discovery cohort, the normalized enrichment score (NES) of the mv-LLG set (−1.88) was lower than that of the mv-HLG set (−1.42), indicating a stronger concordance between the mv-LLG set and LLG. The overall enrichment of CpG sites suggests that the radiogenomic signature derived from the discovery cohort can effectively capture underlying methylation signatures in other cohorts.

Validation of the correlation between DNA methylation signature and prognosis and prediction performance of radiogenomic signature

In the radiomic validation cohort of 122 patients, we examined the correlation between the selected DNA methylation signature (Signature 4) and patient prognosis. We assessed the performance of the radiogenomic signature as a categorical variable for predicting prognosis. Patients were stratified into two groups based on their radiogenomic signature scores, with 91 in HLG and 31 in LLG, respectively. The Kaplan–Meier plot (Fig. 2F) revealed a significant difference in survival between the groups ($P = 0.027$), supporting the potential of the radiogenomic signature as a tool for predicting patient prognosis.

Functional relevance of radiogenomic features at the single-cell level

To gain a deeper understanding of Signature 4 and its potential biological underpinnings, we integrated a previously published scRNA-seq dataset of chordoma with our DNA methylation data. This integration allowed us to investigate the functional relevance of the identified radiogenomic features at the single-cell level. The scRNA-seq dataset, obtained from another study [31], comprised a total of 32,962 cells, which were first categorized into distinct clusters using established clustering methods (not described here, as it is a separate technical detail) and then the tumor cells were distinguished from non-tumor cell types by employing a chordoma-specific marker gene, *TBXT* [43], (Fig. 3A). The non-tumor cell population was further subclustered into specific cell types, including T cells (identified by markers *CD3D*, *CD8A*, and *CD4*), B cells (identified by *CD79A* and *MS4A1*), NK cells (identified by *GNLY* and *NKG7*),

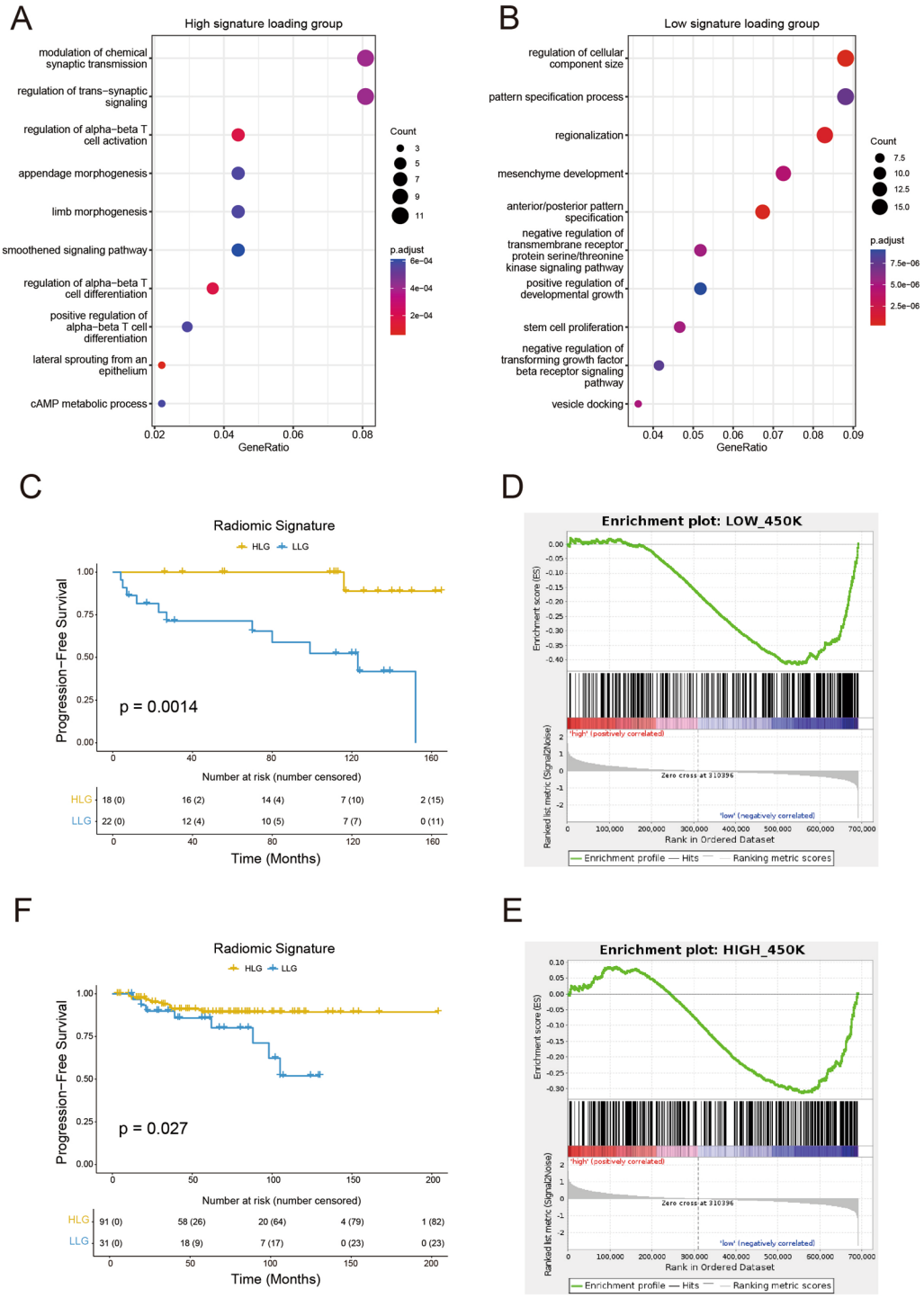

Fig. 2 Characterization of the DNA methylation Signature 4 and prognosis prediction results using the radiogenomic signature. **A**, **B** Biological process functions of genes corresponding to the first 350 most variably methylated sites in both the high- and low-Signature 4 loading groups. **C** Progression-free survival stratified by methylation groups according to the radiogenomic signatures. **D**, **E** Results of GSEA revealing consistency in the CpG sites of the hypomethylated groups between the discovery and validation cohorts. **F** Kaplan–Meier plot illustrating the predictive capacity of the radiomic signature for prognostic risk in 122 patients in the validation cohort

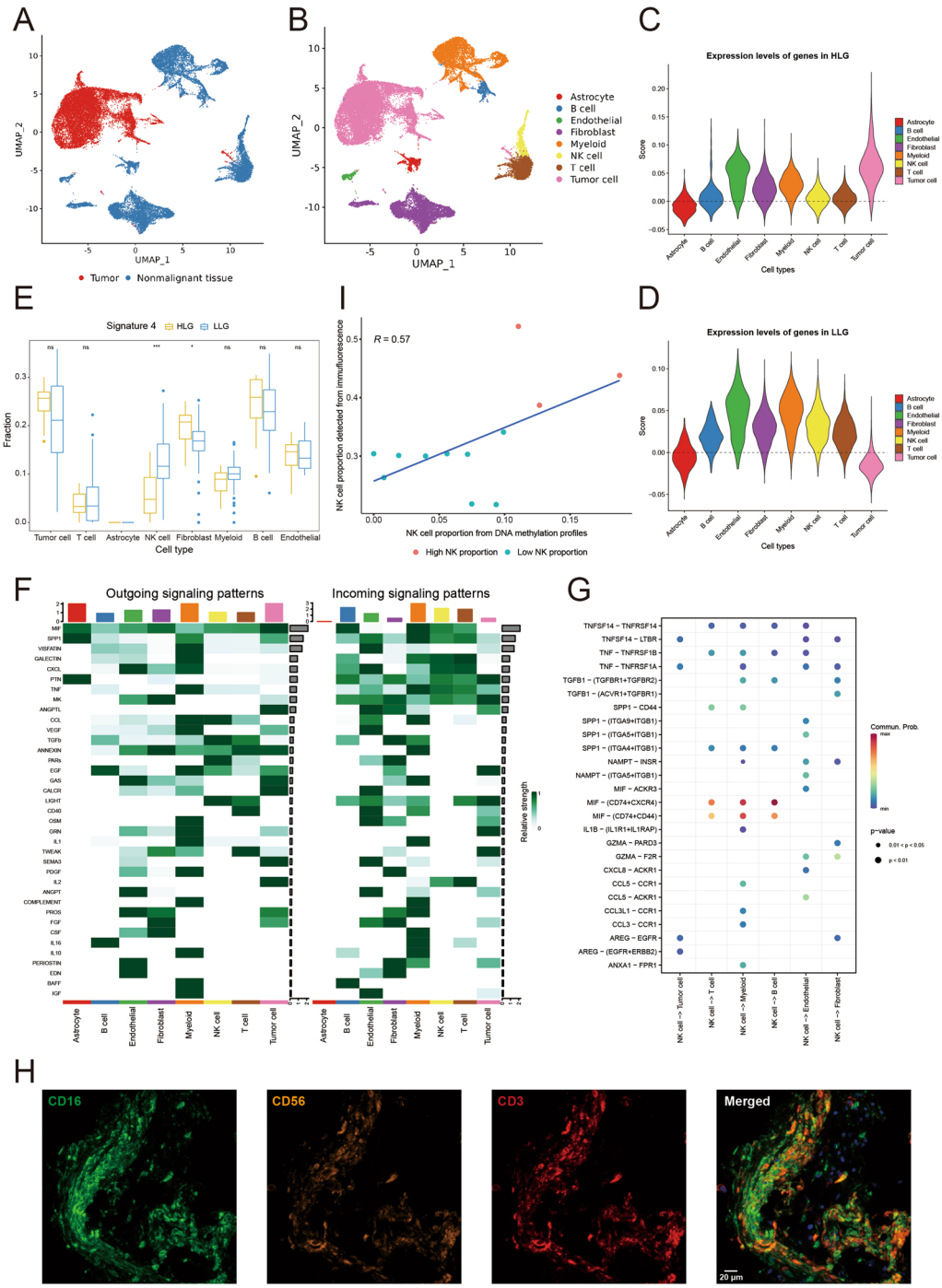

Fig. 3 Integrated analysis of the DNA methylation profile and single-cell transcription profile. **A** UMAP visualization reveals the distribution of tumor cells and adjacent tissues. **B** UMAP visualization of the eight cell types. **C**, **D** Expression of genes corresponding to 1500 methylation sites in the LLG and HLG in single-cell data. **E** Proportions of different cell types in 40 samples obtained using single-cell transcriptional profiles deconvolution DNA methylation profiles. **F** Intercellular signaling pathways across various cell types. **G** Ligand–receptor interaction between NK and other cells. **H** Typical mIHC staining of NK cells. **I** NK cell proportion derived from DNA methylation profiles and mIHC images of 12 samples

myeloid cells (identified by *CD163* and *AIF1*), fibroblasts (identified by *COL3A1*), endothelial cells (identified by *PECAM1*), and astrocytes (Fig. 3B).

We then examined the expression levels of genes associated with differentially methylated CpG sites within the Signature 4 HLG and LLG across these various cell

types. Figure 3C and D depicts the expression patterns of genes derived from the top 1500 differentially methylated CpG sites within each group across different cell types in the scRNA-seq dataset. Interestingly, genes with higher expression in the HLG (likely due to hypomethylation in the HLG) demonstrated elevated expression levels in tumor cells, whereas those with higher expression in the LLG (likely due to hypomethylation in the LLG) showed increased expression in endothelial and myeloid cells.

Difference in cell proportions between the HLG and LLG

To gain further insight into the biological processes underlying Signature 4, we employed a computational technique called deconvolution, which integrates scRNA-seq data with our DNA methylation data to estimate the proportions of different cell types within a tissue sample. Using deconvoluted analysis, we compared the cellular composition of patients categorized by Signature 4 high and low loading values (Fig. 3E). The most significant differences were observed in the proportions of NK cells and fibroblasts. Patients in the HLG exhibited a lower inferred proportion of NK cells, but a significantly higher inferred proportion of fibroblasts, than those in the LLG. These findings suggest a potential link between the proportion of NK cells and fibroblasts and patient prognosis. Further analysis of intercellular communication pathways revealed interactions between NK cells and other cell types. NK cells were predicted to interact with tumor cells through the LIGHT (TNFSF14) pathway and with fibroblasts through the TGF-β pathway (Fig. 3F). Specifically, NK cells appeared to engage in communication via the LIGHT signaling pathway, a member of the TNF-related pathways (Fig. 3G).

To validate the deconvolution results, we employed mIHC to quantify the actual proportion of NK cells in tissue samples from a subset of patients (Fig. 3H). Regions with the highest fluorescence intensity were used to quantify NK cell density. We used the median inferred proportion of NK cells from the DNA methylation profiles as a threshold to categorize samples into high and low NK cell proportion groups. Among the 12 samples analyzed by mIHC, those categorized as having a high NK cell proportion displayed a higher density of NK cells compared with the low NK cell proportion group (Fig. 3I). These findings support the consistency between the inferred NK cell proportion obtained through DNA methylation profiling and the actual cellular composition in tissue samples.

In summary, by integrating DNA methylation data with scRNA-seq data, our study suggests a potential association between NK cells and tumor development in chordoma. We observed significant differences in the inferred proportions of NK cells and fibroblasts between patients categorized by distinct methylation signatures. Furthermore, NK cells were predicted to interact with tumor cells through a pathway potentially linked to tumor suppression. These findings warrant further investigation into the role of NK cells and their interactions with other cell types in the context of chordoma.

Discussion

MRI radiomics has been widely used in clinical diagnostics and proven to be an effective approach for predicting the prognosis of various cancers [44–46]. However, the lack of a clear connection between radiomic features and molecular alterations limits the actionable potential of such predictions. By integrating radiomic features with genomic features, the radiogenomic approach offers a promising solution, combining noninvasive predictive power of radiomics with the interventional potential offered by genomics. In this study, utilizing a radiogenomic strategy, we identified prognosis-specific DNA methylation-associated MRI radiomic features (i.e., radiogenomic signature) in skull base chordoma. The identified radiogenomic signature was not only indicative of differences in PFS among patients but also closely tied to underlying molecular alterations, potentially linked to the activation of TGFB signaling and NK cell proportions.

Our findings indicate the viability of employing radiogenomic analysis outcomes as clinical markers for guiding chordoma treatment. Our radiogenomic signature effectively predicted the specific methylation signatures based solely on MRI image information. Importantly, patients categorized by the radiogenomic signature exhibited significant differences in PFS, highlighting its potential clinical utility. Our analysis of DNA methylation profiles using NMF revealed eight distinct methylation signatures, each representing a unique methylation pattern. Notably, Signature 4 demonstrated a strong association with patient prognosis, suggesting that specific differentially methylated sites within this signature may influence disease course. These findings provide valuable insights for the development of novel treatment strategies. Furthermore, Signature 4 served as a reliable predictor of PFS, which demonstrates the ability of radiogenomics to capture both molecular (DNA methylation) and clinical prognostic features using MRI images. By establishing a link between MRI features and DNA methylation signatures, our study offers a noninvasive approach to assess prognosis in patients with chordoma. This has significant implications for patient management and treatment decisions. However, since obtaining tissue biopsies for DNA methylation analysis is an invasive procedure, we integrated Signature 4 with MRI data to facilitate earlier diagnosis and improve clinical utility. This approach

offers a noninvasive method for detecting and potentially guiding treatment decisions in patients with chordoma.

Radiomic analysis has emerged as a promising tool for improving the effectiveness of image-guided diagnosis and treatment across various cancers. In chordoma research, radiomics has been successfully applied in several areas, including differentiating chordoma from other tumor types [47–49], identifying prognostic markers [50], and assessing prognostic factors for radiotherapy [51]. Our study builds on these advancements by constructing a predictive radiogenomic signature for DNA methylation Signature 4 using radiomic features. This signature allowed us to classify patients based on predicted DNA methylation signature loading values, thereby enabling prognostic risk stratification. In the discovery cohort, the prognostic outcomes of patients classified by the radiogenomic signature were consistent with the original Signature 4 values, indicating that patients in the predicted HLG exhibited better PFS than those in the predicted LLG.

To comprehensively evaluate the generalizability and clinical value of the radiogenomic signature, we recruited an additional 136 patients. Among them, 122 patients had only preoperative MRI images, and their corresponding tissues were unavailable, while the remaining 14 patients had both preoperative MRI images and tissues, but their tissue samples were preserved in FFPE, which may cause changes to DNA methylation. Therefore, these samples were categorized into two validation cohorts to test the performance of the radiogenomic signature. We first hypothesized that DNA methylation signatures are prevalent across patients with chordoma and can be reflected through radiomic features. For the DNA methylation validation cohort, to overcome potential noise from FFPE samples, we employed GSEA to investigate if CpG sites categorized by the radiogenomic signature showed significant enrichment within the HLG and LLG groups of the discovery cohort. The limited sample size of the methylation validation cohort, coupled with potential patient heterogeneity, could significantly impact survival analysis. In our study, the mv-HLG, characterized by radiogenomics signature, comprised 11 patients, whereas the mv-LLG included only three patients. The limited sample size in this cohort would significantly influence the outcome of survival analysis, magnifying the impact of patient distribution disparity. Therefore, in these samples, we did not assess the prognosis of patients after classification using the radiogenomic signature. In the radiogenomic validation cohort comprising 122 samples, we only examined whether the predicted radiogenomic features could effectively differentiate patients with distinct outcomes, due to the unavailability of the corresponding DNA methylation profiles.

We compared differentially methylated sites between the HLG and LLG, which revealed distinct gene functions associated with hypermethylation in each group. In the LLG, negative regulatory genes within the TGF-β pathway were hypermethylated, suggesting a potential inhibition of the pathway's negative regulatory mechanisms, potentially linked to poorer patient prognosis. The TGF-β signaling pathway plays a paradoxical role in cancer progression, functioning as a tumor suppressor in the early stages while transitioning to a tumor promoter in advanced stages. Moreover, the expression level of TGF-β1, a member of the TGF-β family, serves as a prognostic factor for skull base chordoma progression. Patients with high TGF-β1 expression are more prone to tumor recurrence [52]. Similarly, overexpression of BMP4 and Smad, both members of the TGF-β family, has been linked to chordoma development [53]. Therefore, the lack of a negatively regulated TGF-β pathway in the LLG could potentially contribute to a poorer tumor prognosis.

We integrated published scRNA-seq to analyze cell composition within our methylation profiles. Our analysis identified seven cell types, with a significant difference in the proportion of NK cells between the HLG and LLG. Their frequency, infiltration, and functionality influence patient survival [54]. Higher levels of tumor-infiltrating NK cells are associated with a favorable prognosis. However, as tumors progress, they can induce an immunosuppressive microenvironment that hinders NK cell proliferation and function [55]. Interestingly, the HLG had fewer NK cells than the LLG, despite the better prognosis associated with the HLG. This discrepancy may be attributed to the higher tumor cell content in the HLG. As shown in Fig. 3E, the HLG had more tumor cells than the LLG. This higher tumor burden may have led to NK cell depletion during our study. The presence of tumor cells could also impact the metabolism and activation of NK cells, ultimately reducing their numbers. Furthermore, genes associated with the negative regulatory pathway of TGF-β were suppressed in the LLG, potentially leading to elevated TGF-β levels. TGF-β within the tumor microenvironment can impair NK cell function [50] and may correlate with a poorer prognosis in the LLG. Our analysis of cell-to-cell communication using scRNA-seq revealed an interaction between NK and tumor cells through the LIGHT (TNFSF14) signaling pathway. LIGHT/TNFSF14 proteins, belonging to the TNF family, can activate the NF-κB signaling pathway [56], which drives inflammatory responses in cancers and exhibits a pro-tumorigenic function [57]. We observed ligand–receptor interactions involving the LIGHT protein and its two receptors, TNFRSF14 and LTβR, both of which are associated with anti-tumor responses. LIGHT-TNFRSF14 signaling is responsible for the immune-stimulating properties of

LIGHT. LIGHT produced by tumor-sensing NK cells is a critical component in the NK-DC crosstalk, which plays a role in priming anti-tumor responses [58]. LTβR serves dual roles, both inhibiting and promoting tumor growth. Tumor cells expressing LTβR can be eliminated by LIGHT-expressing cells or induce the production of chemokines to recruit immune cells expressing LIGHT [59]. Thus, our findings indicate that in patients with chordoma, the proportion of NK cells influences patient prognosis. In the tumor microenvironment, NK cells interact with tumor cells through the LIGHT signaling pathway. However, the underlying mechanisms behind these interactions require further investigation.

We assessed the presence of differences in the proportion of NK cells in patient tissue samples using mIHC. The samples were divided into two groups based on the inferred proportion of NK cells from their DNA methylation profiles. One group had an inferred NK cell proportion greater than the median of 40 samples, and the other had a proportion less than the median. Samples with a higher inferred proportion of NK cells also exhibited a larger proportion of NK cells in the actual mIHC images, demonstrating a positive correlation between the inferred and actual measured proportions of NK cells. However, the ranking of samples based on the predicted NK cell proportions did not consistently align with that based on the actual NK cell proportions. This discrepancy may be due to variations in cell distribution within different sections of the same sample. Additionally, the small sample size of the study indicates that individual variations have a more pronounced impact. Overall, differences in the inferred proportions of NK cells from the patients' DNA methylation profiles are reflected in the actual conditions.

In summary, we presented a noninvasive radiogenomic approach to predict DNA methylation signatures and prognostic traits of patients with chordoma. Using this approach, we developed a radiogenomic signature. This approach has the potential to uncover novel biomarkers that could improve routine patient management. However, some limitations require further investigation. First, the sample size was limited by the low incidence of chordoma, potentially hindering the generalizability of our findings. Second, the lack of tissue samples from early-stage patients prevented the analysis of DNA methylation in this crucial stage, thus impeding the validation of our results. Third, the limited sample size currently restricts our ability to accurately predict PFS directly. Furthermore, the functional role of NK cells in chordoma remains unexplored due to the absence of experimental investigations. Future studies will address these limitations by expanding the sample size and strengthening the verification of analysis results. Additionally, we aim to develop methods for directly predicting patient PFS based on the outcomes of radiogenomic analysis.

Conclusion

This study identified a prognostic DNA methylation signature in skull base chordoma patients. We further established an MRI-based radiogenomic signature for noninvasive assessment of this methylation signature and prognostic classification. The proportion of NK cells correlated with the DNA methylation signature, potentially influencing patient outcomes. Additionally, the detection of interactions within the LIGHT signaling pathway between NK cells and tumor cells suggests a promising therapeutic target. This method effectively predicted the DNA methylation signature and prognostic risk associated with chordoma. By enhancing our understanding of the molecular landscape of chordoma, this study offers a valuable tool for clinicians to guide treatment decisions and evaluate prognoses for patients with this disease.

Abbreviations

MRI	Magnetic resonance imaging
FFPE	Formalin-fixed paraffin-embedded
NMF	Nonnegative matrix factorization
PFS	Progression-free survival
FDR	False discovery rate
DMPs	Differentially methylated probes
mIHC	Multiplex immunofluorescence histochemistry
GSEA	Gene set enrichment analysis
LLG	Low-signature loading group
HLG	High-signature loading group
mv-HLG	Methylation validation high signature loading group
mv-LLG	Methylation validation low signature loading group

Supplementary Information

The online version contains supplementary material available at https://doi.org/10.1186/s13148-025-01836-w.

Supplementary Material 1

Supplementary Material 2

Acknowledgements

The authors would like to thank Dr. Guanglei Zhang and Fan Song from Beihang University for their support in radiomic features analysis. We also thank TopEdit (www.topeditsci.com) for its linguistic assistance during the preparation of this manuscript.

Author contributions

Deng XY performed the radiogenomics modeling, analyzed the data, and wrote and revised the manuscript; Li PR and Tian KB conducted the sample collection and diagnosis, analyzed the radiomic data, and performed mIHC experiments; Zhang F and Yan YM analyzed the genomics data; Fan YH analyzed the radiomic data; Wu Z and Zhang JT supervised the study; Du J, Chen W, and Wang L designed, supervised, analyzed the data, and revised the manuscript.

Funding

The study was supported by National Natural Science Foundation of China grants 82141113 and 82373116; and Beijing Natural Science Foundation grant 5232014.

Availability of data and materials
The datasets analyzed during the current study are available from the corresponding author on reasonable request.

Declarations

Ethics approval and consent to participate
This study was conducted in accordance with the principles of the Declaration of Helsinki and was approved by the ethics committees of the Beijing Tiantan Hospital. All patients gave their informed consent in writing and the ethics committees approved the consent procedure.

Competing interests
The authors declare that the research was conducted in the absence of any commercial or financial relationships that could be construed as a potential conflict of interest.

Author details
[1]Key Laboratory of Biomechanics and Mechanobiology (Beihang University), Ministry of Education; Key Laboratory of Innovation and Transformation of Advanced Medical Devices, Ministry of Industry and Information Technology; National Medical Innovation Platform for Industry-Education Integration in Advanced Medical Devices (Interdiscipline of Medicine and Engineering); School of Engineering Medicine, Beihang University, Beijing, China. [2]Department of Neurosurgery, Beijing Tiantan Hospital, Capital Medical University, Beijing, China. [3]Beijing Neurosurgical Institute Capital Medical University, Beijing, China.

Received: 15 October 2024 Accepted: 6 February 2025
Published online: 17 February 2025

References

1. Wedekind MF, Widemann BC, Cote G. Chordoma: current status, problems, and future directions. Curr Probl Cancer. 2021;45(4): 100771.
2. Karele EN, Paze AN. Chordoma: to know means to recognize. Biochim Biophys Acta Rev Cancer. 2022;1877(5): 188796.
3. Walcott BP, Nahed BV, Mohyeldin A, Coumans JV, Kahle KT, Ferreira MJ. Chordoma: current concepts, management, and future directions. Lancet Oncol. 2012;13(2):e69-76.
4. Zhou L, Huang R, Wei Z, Meng T, Yin H. The clinical characteristics and prediction nomograms for primary spine malignancies. Front Oncol. 2021;11: 608323.
5. Williams BJ, Raper DM, Godbout E, Bourne TD, Prevedello DM, Kassam AB, et al. Diagnosis and treatment of chordoma. J Natl Compr Canc Netw. 2013;11(6):726–31.
6. Meng T, Yin H, Li B, Li Z, Xu W, Zhou W, et al. Clinical features and prognostic factors of patients with chordoma in the spine: a retrospective analysis of 153 patients in a single center. Neuro Oncol. 2015;17(5):725–32.
7. Karpathiou G, Dumollard JM, Dridi M, dal Col P, Barral FG, Boutonnat J, et al. Chordomas: a review with emphasis on their pathophysiology, pathology, molecular biology, and genetics. Pathol Res Pract. 2020;216(9): 153089.
8. Zhu GG, Ramirez D, Chen W, Lu C, Wang L, Frosina D, et al. Chromosome 3p loss of heterozygosity and reduced expression of H3K36me3 correlate with longer relapse-free survival in sacral conventional chordoma. Hum Pathol. 2020;104:73–83.
9. Scheil-Bertram S, Kappler R, von Baer A, Hartwig E, Sarkar M, Serra M, et al. Molecular profiling of chordoma. Int J Oncol. 2014;44(4):1041–55.
10. Sa JK, Lee IH, Hong SD, Kong DS, Nam DH. Genomic and transcriptomic characterization of skull base chordoma. Oncotarget. 2017;8(1):1321–8.
11. Bell AH, DeMonte F, Raza SM, Rhines LD, Tatsui CE, Prieto VG, et al. Transcriptome comparison identifies potential biomarkers of spine and skull base chordomas. Virchows Arch. 2018;472(3):489–97.
12. Bell D, Raza SM, Bell AH, Fuller GN, DeMonte F. Whole-transcriptome analysis of chordoma of the skull base. Virchows Arch. 2016;469(4):439–49.
13. Zhang K, Chen H, Wu G, Chen K, Yang H. High expression of SPHK1 in sacral chordoma and association with patients' poor prognosis. Med Oncol. 2014;31(11):247.
14. Ma J, Tian K, Du J, Wu Z, Wang L, Zhang J. High expression of survivin independently correlates with tumor progression and mortality in patients with skull base chordomas. J Neurosurg. 2020;132(1):140–9.
15. Thanindratarn P, Dean DC, Feng W, Wei R, Nelson SD, Hornicek FJ, et al. Cyclin-dependent kinase 12 (CDK12) in chordoma: prognostic and therapeutic value. Euro Spin J Off Publ Euro Spin Soc Euro Spin Deformity Soc Euro Sect Cerv Spin Res Soc. 2020;29(12):3214–28.
16. Papanicolau-Sengos A, Aldape K. DNA methylation profiling: an emerging paradigm for cancer diagnosis. Annu Rev Pathol. 2022;17:295–321.
17. Huo X, Guo T, Wang K, Yao B, Li D, Li H, et al. Methylation-based reclassification and risk stratification of skull-base chordomas. Front Oncol. 2022;12: 960005.
18. Zuccato JA, Patil V, Mansouri S, Liu JC, Nassiri F, Mamatjan Y, et al. DNA methylation-based prognostic subtypes of chordoma tumors in tissue and plasma. Neuro Oncol. 2022;24(3):442–54.
19. Alholle A, Brini AT, Bauer J, Gharanei S, Niada S, Slater A, et al. Genome-wide DNA methylation profiling of recurrent and non-recurrent chordomas. Epigenetics. 2015;10(3):213–20.
20. Kirienko M, Sollini M, Corbetta M, Voulaz E, Gozzi N, Interlenghi M, et al. Radiomics and gene expression profile to characterise the disease and predict outcome in patients with lung cancer. Eur J Nucl Med Mol Imaging. 2021;48(11):3643–55.
21. Yamamoto S, Korn RL, Oklu R, Migdal C, Gotway MB, Weiss GJ, et al. ALK molecular phenotype in non-small cell lung cancer: CT radiogenomic characterization. Radiology. 2014;272(2):568–76.
22. Yamamoto S, Maki DD, Korn RL, Kuo MD. Radiogenomic analysis of breast cancer using MRI: a preliminary study to define the landscape. AJR Am J Roentgenol. 2012;199(3):654–63.
23. Han L, Wang S, Miao Y, Shen H, Guo Y, Xie L, et al. MRI texture analysis based on 3D tumor measurement reflects the IDH1 mutations in gliomas—a preliminary study. Eur J Radiol. 2019;112:169–79.
24. Zhang X, Tian Q, Wu Y-X, Xu X-P, Li B-J, Liu Y-X, et al. IDH mutation assessment of glioma using texture features of multimodal MR images: SPIE; 2017.
25. Zhang L, Chen B, Liu X, Song J, Fang M, Hu C, et al. Quantitative biomarkers for prediction of epidermal growth factor receptor mutation in non-small cell lung cancer. Transl Oncol. 2018;11(1):94–101.
26. Morris TJ, Butcher LM, Feber A, Teschendorff AE, Chakravarthy AR, Wojdacz TK, et al. ChAMP: 450k chip analysis methylation pipeline. Bioinformatics. 2013;30(3):428–30.
27. Tian Y, Morris TJ, Webster AP, Yang Z, Beck S, Feber A, et al. ChAMP: updated methylation analysis pipeline for Illumina BeadChips. Bioinformatics. 2017;33(24):3982–4.
28. Gaujoux R, Seoighe C. A flexible R package for nonnegative matrix factorization. BMC Bioinform. 2010;11(1):367.
29. Kassambara A, Kosinski M, Biecek P, editors. Drawing survival curves using 'ggplot2' [R package survminer version 0.4.8] 2020.
30. Wu T, Hu E, Xu S, Chen M, Guo P, Dai Z, et al. clusterProfiler 4.0: A universal enrichment tool for interpreting omics data. In: The innovation. 2021; 2(3).
31. van Griethuysen JJM, Fedorov A, Parmar C, Hosny A, Aucoin N, Narayan V, et al. Computational radiomics system to decode the radiographic phenotype. Can Res. 2017;77(21):e104–7.
32. Sztepanacz JL, Houle D. Regularized regression can improve estimates of multivariate selection in the face of multicollinearity and limited data. Evolut Lett. 2024;8(3):361–73.
33. Yadav S, Shukla S. Analysis of k-fold cross-validation over hold-out validation on colossal datasets for quality classification. In: 2016 IEEE 6th international conference on advanced computing (IACC) 2016; 78–83.
34. Pedregosa F, Varoquaux G, Gramfort A, Michel V, Thirion B, Grisel O, et al. Scikit-learn: machine learning in python. J Mach Learn Res. 2011;12:2825–30.
35. Mootha VK, Lindgren CM, Eriksson KF, Subramanian A, Sihag S, Lehar J, et al. PGC-1alpha-responsive genes involved in oxidative phosphorylation are coordinately downregulated in human diabetes. Nat Genet. 2003;34(3):267–73.
36. Subramanian A, Tamayo P, Mootha VK, Mukherjee S, Ebert BL, Gillette MA, et al. Gene set enrichment analysis: a knowledge-based approach for

interpreting genome-wide expression profiles. Proc Natl Acad Sci USA. 2005;102(43):15545–50.
37. Duan WR, Zhang BY, Li XQ, Chen W, Jia SH, Xin Z, et al. Single-cell transcriptome profiling reveals intra-tumoral heterogeneity in human chordomas. Cancer Immunol Immunother. 2022;71(9):2185–95.
38. Hao Y, Hao S, Andersen-Nissen E, Mauck WM 3rd, Zheng S, Butler A, et al. Integrated analysis of multimodal single-cell data. Cell. 2021;184(13):3573-87.e29.
39. Aran D, Looney AP, Liu L, Wu E, Fong V, Hsu A, et al. Reference-based analysis of lung single-cell sequencing reveals a transitional profibrotic macrophage. Nat Immunol. 2019;20(2):163–72.
40. Jin S, Guerrero-Juarez CF, Zhang L, Chang I, Ramos R, Kuan CH, et al. Inference and analysis of cell-cell communication using cell chat. Nat Commun. 2021;12(1):1088.
41. Teschendorff AE, Zhu T, Breeze CE, Beck S. EPISCORE: cell type deconvolution of bulk tissue DNA methylomes from single-cell RNA-Seq data. Genome Biol. 2020;21(1):221.
42. Schindelin J, Arganda-Carreras I, Frise E, Kaynig V, Longair M, Pietzsch T, et al. Fiji: an open-source platform for biological-image analysis. Nat Method. 2012;9(7):676–82.
43. Zhang Q, Fei L, Han R, Huang R, Wang Y, Chen H, et al. Single-cell transcriptome reveals cellular hierarchies and guides p-EMT-targeted trial in skull base chordoma. Cell Discov. 2022;8(1):94.
44. Li G, Li L, Li Y, Qian Z, Wu F, He Y, et al. An MRI radiomics approach to predict survival and tumour-infiltrating macrophages in gliomas. Brain. 2022;145(3):1151–61.
45. Wang X-H, Long L-H, Cui Y, Jia AY, Zhu X-G, Wang H-Z, et al. MRI-based radiomics model for preoperative prediction of 5-year survival in patients with hepatocellular carcinoma. Br J Cancer. 2020;122(7):978–85.
46. Chen BT, Jin T, Ye N, Mambetsariev I, Wang T, Wong CW, Salgia R. Predicting survival duration with MRI radiomics of brain metastases from non-small cell lung cancer. Front Oncol. 2021;11:621088.
47. Li LF, Wang K, Ma XJ, Liu ZY, Wang S, Du J, et al. Radiomic analysis of multiparametric magnetic resonance imaging for differentiating skull base chordoma and chondrosarcoma. Eur J Radiol. 2019;118:81–7.
48. Yamazawa E, Takahashi S, Shin M, Tanaka S, Takahashi W, Nakamoto T, et al. MRI-based radiomics differentiates skull base chordoma and chondrosarcoma: a preliminary study. Cancers. 2022;14(13):3264.
49. Yin P, Mao N, Wang SC, Sun C, Hong N. Clinical-radiomics nomograms for pre-operative differentiation of sacral chordoma and sacral giant cell tumor based on 3D computed tomography and multiparametric magnetic resonance imaging. Br J Radiol. 2019;92(1101):20190155.
50. Wei W, Wang K, Liu Z, Tian K, Wang L, Du J, et al. Radiomic signature: a novel magnetic resonance imaging-based prognostic biomarker in patients with skull base chordoma. Radiother Oncol. 2019;141:239–46.
51. Buizza G, Paganelli C, D'Ippolito E, Fontana G, Molinelli S, Preda L, et al. Radiomics and dosiomics for predicting local control after carbon-ion radiotherapy in skull-base chordoma. Cancers. 2021;13(2):339.
52. Ma J, Tian K, Wang L, Wang K, Du J, Li D, et al. High Expression of TGF-beta1 predicting tumor progression in skull base chordomas. World Neurosurg. 2019;131:e265–70.
53. Feng Y, Zhang Q, Wang Z, Yan B, Wei W, Li P. Overexpression of the BMP4/SMAD signaling pathway in skull base chordomas is associated with poor prognosis. Int J Clin Exp Pathol. 2015;8(7):8268–75.
54. Huntington ND, Cursons J, Rautela J. The cancer-natural killer cell immunity cycle. Nat Rev Cancer. 2020;20(8):437–54.
55. Melaiu O, Lucarini V, Cifaldi L, Fruci D. Influence of the tumor microenvironment on NK cell function in solid tumors. Front Immunol. 2019;10:3038.
56. Aggarwal BB. Signalling pathways of the TNF superfamily: a double-edged sword. Nat Rev Immunol. 2003;3(9):745–56.
57. Taniguchi K, Karin M. NF-kappaB, inflammation, immunity and cancer: coming of age. Nat Rev Immunol. 2018;18(5):309–24.
58. Skeate JG, Otsmaa ME, Prins R, Fernandez DJ, Da Silva DM, Kast WM. TNFSF14: LIGHTing the way for effective cancer immunotherapy. Front Immunol. 2020;11:922.
59. Fernandes MT, Dejardin E, dos Santos NR. Context-dependent roles for lymphotoxin-beta receptor signaling in cancer development. Biochim Biophys Acta. 2016;1865(2):204–19.

Publisher's Note